

MAGIC: Mask-Guided Diffusion Inpainting with Multi-Level Perturbations and Context-Aware Alignment for Few-Shot Anomaly Generation

JaeHyuck Choi¹ MinJun Kim² JeHyeong Hong^{2,*}

¹Department of Artificial Intelligence Semiconductor Engineering, Hanyang University

²Department of Electronic Engineering, Hanyang University

{sunhp1333, ihatelemon, jhh37}@hanyang.ac.kr

Abstract

Few-shot anomaly generation is emerging as a practical solution for augmenting the scarce anomaly data in industrial quality control settings. An ideal generator would meet three demands at once, namely (i) keep the normal background intact, (ii) inpaint anomalous regions to tightly overlap with the corresponding anomaly masks, and (iii) generate anomalous regions in a semantically valid location, while still producing realistic, diverse appearances from only a handful of real examples. Existing diffusion-based methods usually satisfy at most two of these requirements: global anomaly generators corrupt the background, whereas mask-guided ones often falter when the mask is imprecise or misplaced. We propose MAGIC—Mask-guided inpainting with multi-level perturbations and Context-aware alignment—to resolve all three issues. At its core, MAGIC fine-tunes a Stable Diffusion inpainting backbone that preserves normal regions and ensures strict adherence of the synthesized anomaly to the supplied mask, directly addressing background corruption and misalignment. To offset the diversity loss that fine-tuning can cause, MAGIC adds two complementary perturbation strategies: (i) Gaussian prompt-level perturbation applied during fine-tuning and inference that broadens the global appearance of anomalies while avoiding low-fidelity textual appearances, and (ii) mask-guided spatial noise injection that enriches local texture variations. Additionally, the context-aware mask alignment module forms semantic correspondences and relocates masks so that every anomalies remains plausibly contained within the host object, eliminating out-of-boundary artifacts. Under a consistent identical evaluation protocol on the MVTec-AD dataset, MAGIC outperforms previous state-of-the-arts in downstream anomaly tasks. Code is available at <https://github.com/Jaeihk/MAGIC-Anomaly-generation>.

1 Introduction

In the manufacturing industry, automatic detection, localization, and classification of anomalies are essential for quality control and yield improvement [18, 40]. However, practitioners face an inherent data imbalance: normal images are abundant while images depicting anomalies are scarce. Although prior studies [28] have shown that anomaly detection and localization can be achieved using only normal-image training (e.g., one-class classification or reconstruction-based methods), accurate anomaly classification which is crucial for root-cause analysis, still requires labeled anomaly examples. To fill this gap, recent studies have turned to generative models that synthesize realistic anomalous images with the aim of supplying data for downstream classifiers [10].

*Corresponding author.

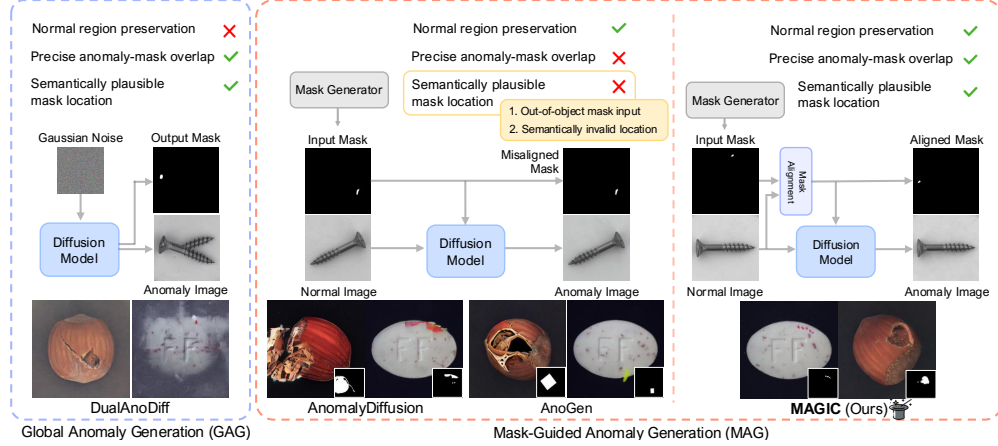


Figure 1: Characteristics and failure modes of existing anomaly generators. Global Anomaly Generation (GAG) does not involve normal image guidance during inference and consequently often corrupts (normal) background textures. Mask-guided Anomaly Generation (MAG) keeps the background intact but (i) misaligns the synthesized anomaly with the input mask and (ii) produces low-fidelity anomalies when the mask is misplaced in semantically invalid regions (e.g., a *scratch_head* anomaly on a screw must lie on the screw-head but generated masks frequently miss that region when the screws are rotated.) Our framework eliminates both issues, preserving background fidelity while producing mask-accurate, high-fidelity anomalies even under imperfect mask input.

Existing anomaly generation methods can be divided into two groups. The Global Anomaly Generation (GAG) methods (e.g., [11]) generate anomaly images and masks simultaneously without requiring an input mask that specifies the anomaly region. While this is empirically observed to generate semantically diverse anomaly images, normal regions are often not preserved which can substantially degrade the realism of the generated image. (Fig. 1). In contrast, Mask-guided Anomaly Generation (MAG) approaches utilize normal image and a user-provided mask to designate the anomaly region [36, 16, 35, 10, 7, 1]. While the background is now well-preserved, MAG-based methods [7, 10] often exhibit weaknesses such as misalignment of input mask and synthesized anomaly region and generated masks straying outside the object boundary. To the best of our knowledge, there is no algorithm that can address these limitations of both approaches simultaneously.

In this work, we tackle the three chronic weaknesses of few-shot anomaly generators—(i) loss of background fidelity, (ii) non-overlap between a supplied mask and synthesized anomaly, and (iii) masks or anomalies that misalign—within a single framework. For this purpose, we propose MAGIC, a novel mask-guided anomaly generation framework based on a Stable Diffusion inpainting model, fine-tuned via DreamBooth [29]. Our motivation is that inpainting the anomaly regions to normal images can effectively preserve the normal background while enforcing anomalies to abide by the input masks, directly addressing i) and ii). Yet naively fine-tuning on few anomaly examples leads to overfitting (visual repetition and limited diversity as also discussed in previous literatures [15, 43]) while still failing whenever a user-provided or generated anomaly mask lies in an implausible location. To overcome these two remaining problems, we add three modules that inject diversity and enforce semantic plausibility, yielding the following contributions:

- **MAGIC Framework.** A mask-guided anomaly generator that fine-tunes Stable Diffusion inpainting with DreamBooth without requiring object-specific textual prompts, preserving normal backgrounds and aligning anomalies to the input mask.
- **Gaussian Prompt Perturbation (GPP).** During both training and inference, we inject Gaussian noise into the anomaly-token embedding, broadening the diversity of global textural appearance of anomalous regions while retaining realism.
- **Mask-Guided Noise Injection (MGNI).** We apply spatially confined, gradually decaying stochastic noise to the masked region during DDIM sampling, enriching local texture diversity yet leaving normal pixels mainly untouched.
- **Context-Aware Mask Alignment (CAMA).** Leveraging semantic correspondences, CAMA relocates an input mask to the most plausible object part, preventing out-of-object artifacts and semantically invalid regions.

Additionally, we faithfully reproduce every competing method and evaluate them under an identical protocol in [10], demonstrating that MAGIC outperforms previous state-of-the-arts on the MVTecAD [2] dataset on downstream tasks (anomaly detection, localization, and classification).

2 Related work

2.1 Anomaly generation

Hand-crafted augmentation. Early work framed anomaly synthesis purely as data augmentation. Crop-Paste [17] transfers segmented anomalies to normal images, whereas CutPaste [16] creates anomalous region without utilizing real anomalies by copy-pasting patches from the same image. DRAEM [36] and Prototypical Residual Networks (PRN) [38] overlay Perlin noise; PRN further borrows textures from DTD-Synthetic [4]. As none of these methods model the full image distribution, their anomalies remain geometrically or photometrically inconsistent, limiting realism and diversity.

GAN-based generators. To overcome those limits, researchers adopted generative adversarial networks (GANs). SDGAN [22] adds cycle-consistency between normal and anomalous domain, stabilizing training but coupling each normal image to a single defect, reducing diversity and corrupting backgrounds. Defect-GAN [37] injects layer-wise stochastic noise to widen appearance variation, and DFMGAN [5] builds on a pre-trained StyleGAN2 [13] to improve fidelity. Yet GANs still suffer from mode collapse and gradient instability [20, 14], especially when only a few anomaly exemplars are available, leading to limited diversity.

Diffusion-based generators. Diffusion models now dominate high-fidelity image synthesis. The GAG-style DualAnoDiff [11] runs two attention-sharing streams—one for the whole image, one for the anomaly patch, being capable of generating realistic and diverse anomaly images. Unfortunately, since it regenerates the entire image without mask conditioning, background textures can change undesirably, yielding unrealistic artifacts. On the other hand, mask-guided (MAG) approaches, such as AnoGen [7] and AnomalyDiffusion [10], keep the diffusion backbone frozen and use textual inversion [6] and an input mask to locate anomaly. Mask conditioning preserves normal regions and gives coarse spatial control, but the frozen backbone restricts quality of anomaly textures and inaccurate anomaly masks produce low-fidelity results or spill beyond object boundaries.

Concurrent work. The very recent DefectFill [32] also fine-tunes an inpainting diffusion model, but differs from our approach in three ways: (i) it requires an object-specific textual prompt during training (e.g. “hazelnut”), reducing applicability to industrial parts lacking descriptive labels; (ii) diversity remains limited, a known issue for fine-tuned inpainting models [34, 19]; and (iii) like other MAG-based methods, it cannot prevent misplaced anomaly masks from degrading fidelity, leaving certain object categories involving substantial geometric transformations (translation, rotation) unsupported. These gaps in diversity and spatial precision motivate the design choices in MAGIC.

2.2 Personalized diffusion models

State-of-the-art text-to-image diffusion backbones (Stable Diffusion, Imagen, GLIDE, etc.) [26, 31, 21, 41] deliver high fidelity but struggle to reproduce a new subject from only a few reference images. Embedding-based methods leave the backbone frozen: Textual inversion [6] learns a single pseudo-token, and DreamDistribution [42] extends this to a distribution of soft-prompt embeddings, gaining diversity but often lacking subject-specific details for images from narrow specific domains.

DreamBooth [29] instead fine-tunes the entire model so a rare identifier token maps to the target concept, achieving the best fidelity yet prone to overfitting and reduced diversity. This motivates our work to adopt a DreamBooth-tuned (inpainting) backbone for high fidelity, then presenting modules to restore diversity and enforce spatial precision of generated images.

3 Method

We review the preliminaries and illustrate each component of our method (see Fig. 2 for an overview).

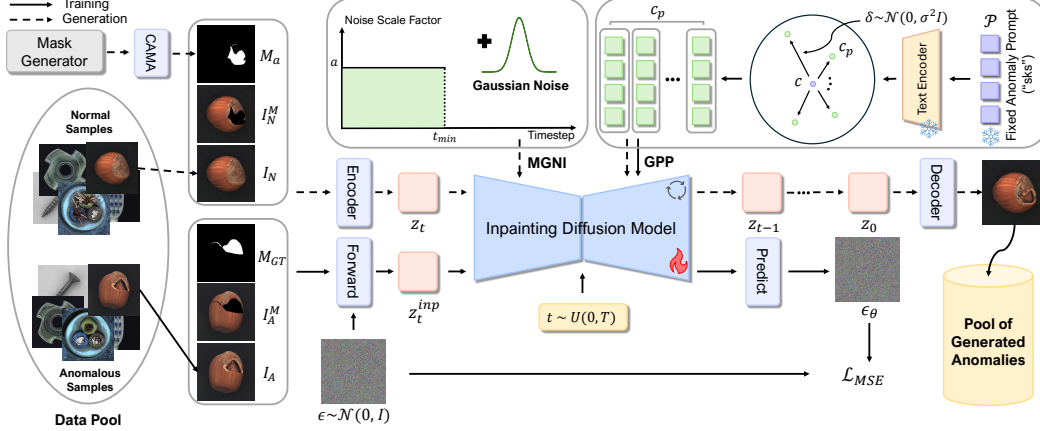


Figure 2: **Framework overview.** A fixed anomaly prompt \mathcal{P} (e.g., “sks”) undergoes Gaussian prompt perturbation (GPP) to create c_p during both training and inference with the aim of diversifying global-scale anomaly texture appearance without compromising realism. In training, an inpainting diffusion backbone receives an anomaly image I_A , ground-truth mask M_{GT} , and masked input I_A^M , all conditioned on (perturbed) c_p , so the network learns to fill the masked region while keeping the background. At inference, a normal image I_N and automatically generated (or user-input) mask M are refined by Context-Aware Mask Alignment (CAMA) to yield a semantically plausible mask M_a . Generation is driven by another randomly perturbed c_p and further diversified by Mask-Guided Noise Injection (MGNI), which inserts localized noise inside M_a with a strength factor a that decays over denoising steps, enriching patch-level anomaly texture without disturbing the background.

3.1 Preliminaries

Text-to-image diffusion models. Diffusion models are generative models that transform samples drawn from a Gaussian noise distribution into realistic data through an iterative denoising process. In text-to-image generation, a text encoder τ maps a prompt \mathcal{P} to a conditioning vector $c = \tau(\mathcal{P})$, which guides the image generation process. Latent Diffusion Models (LDMs) [26] extend this framework by operating in a lower-dimensional latent space for efficiency. A pretrained encoder \mathcal{E} maps an image x to a latent representation $z_0 = \mathcal{E}(x)$, and a decoder \mathcal{D} reconstructs the image via $x \approx \mathcal{D}(z_0)$. Given a dataset $\mathcal{D} = \{(x, c)\}$ of image-text pairs, the model learns the conditional distribution $p(x|c)$. At each diffusion step t , Gaussian noise $\epsilon \sim \mathcal{N}(0, I)$ is added to the latent z_0 to obtain z_t . Then, training involves finding the set of diffusion model weights θ which minimizes

$$\mathcal{L}_{\text{LDM}} = \mathbb{E}_{z_t, \epsilon, t} \left[\|\epsilon - \epsilon_\theta(z_t, t, c)\|_2^2 \right], \quad (1)$$

where ϵ_θ is the noise predicted by the latent diffusion model at time step t provided z_t and c .

Inpainting diffusion models. Inpainting with LDMs involves synthesizing plausible content in missing regions of a given image. For this purpose, the denoising process is now additionally conditioned on the background-only image B (with the anomaly region masked out) with its latent representation $b = \mathcal{E}(B)$ and a binary mask M . Training the model with this background conditioning can simply be achieved by forming a concatenated latent representation $z_t^{\text{inp}} := \text{concat}(z_t, b, M)$ then minimize the same loss as in Eq. (1) with the exception of replacing z_t by z_t^{inp} . Our method employs the stable diffusion-based inpainting backbone [26] with Dreambooth fine-tuning [29].

Diffusion-based anomaly mask generation. AnomalyDiffusion [10] automatically generates anomaly masks by learning the real mask distribution through a trainable mask embedding $[V_m^*]$, which is used as the text condition to guide the diffusion process. Since this is carried out via textual inversion [6], the optimal mask embedding $[V_m^*]$ is obtained by minimizing Eq. (1) except c is replaced by learnable $[V_m^*]$ and the diffusion model weights θ remain fixed. Once trained, the learned embedding enables generation of varied and plausible anomaly masks without relying on real mask annotations. In our method, we also use the same mask generation approach for anomaly synthesis.

3.2 Gaussian prompt perturbation (GPP)

GPP injects Gaussian noise into prompt embedding during both training and inference stages to introduce global but realistic variability of textures in synthesized anomaly regions. After we set

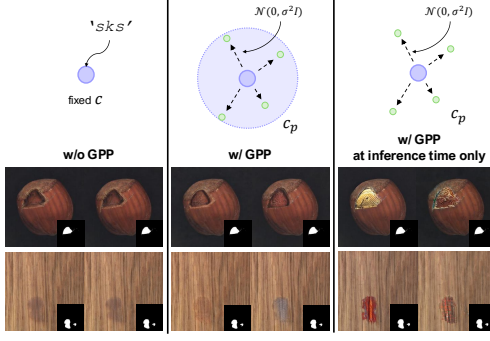


Figure 3: Effect of Gaussian Prompt Perturbation (GPP) shown on two different noise seeds. Applying GPP at both training and test times broadens the global textural appearance of anomalies while avoiding unrealistic textures.

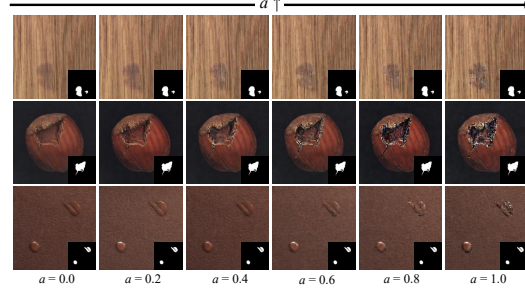


Figure 4: Effect of Mask-Guided Noise Injection (MGNI) as a function of the noise scale a . Since higher a yields more drastic changes in the anomaly texture, we sample a from between 0.0 and 0.6 for controlled variability.

a fixed anomaly prompt \mathcal{P} (e.g., a rare token such as "sks" to minimize semantic bias and solely represent anomaly concept) and map to an embedding $c = \tau(\mathcal{P})$, the perturbed embedding c_p is

$$c_p := \tilde{\tau}(\mathcal{P}) = \tau(\mathcal{P}) + \delta, \quad \delta \sim \mathcal{N}(0, \sigma^2 I), \quad (2)$$

where σ controls the perturbation scale. c_p is then provided as a condition for the stable diffusion-based inpainting backbone with each latent $z_t^{\text{inp}} = \text{concat}(z_t, b_A, M_{GT})$, where z_t is the latent at time step t , M_{GT} is the ground truth anomaly mask and b_A is the encoded masked (normal) background of the anomaly image I_A such that $b_A = \mathcal{E}(I_A^M)$ with $I_A^M := (1 - M_{GT}) \odot I_A$.

We observed that applying Gaussian Prompt Perturbation (GPP) only at test time increases diversity, but it also produces visibly unrealistic textures (last column of Fig. 3). The likely cause is a distribution shift: at inference, the diffusion model receives perturbed prompt embeddings it never encountered during training. We therefore introduce GPP during training as well, essentially mapping anomaly images with a ball of noisy prompt embeddings rather than a single, fixed token. By seeing many nearby embeddings that correspond to slightly different anomaly textures, the model learns a smoother mapping from the embedding space to image space. At test time, sampling from that same ball now yields diverse yet realistic anomalies, because the model has already interpolated across similar embeddings during training. This can be achieved by minimizing

$$\mathcal{L}_{\text{GPP}} = \mathbb{E}_{z_t^{\text{inp}}, t, \epsilon} [\|\epsilon - \epsilon_\theta(z_t^{\text{inp}}, t, c_p)\|_2^2]. \quad (3)$$

As shown in Fig. 3, this strategy significantly diversifies the global textural appearance of the anomaly region without compromising realism when compared with simply changing the noise seed.

3.3 Mask-guided spatial noise injection (MGNI)

To further increase patch-level diversity of anomaly regions during denoising, MGNI employs a DDIM scheduler [33] that selectively injects spatially localized noise into masked regions using a binary mask and a time-dependent decay schedule. This time-dependent noise scheduling is inspired by prior works that anneal perturbations in the conditioning space [30], but MGNI applies it to the image latent space in a localized manner.

At inference time, the model takes a normal image I_N , a binary anomaly mask M_a , and the masked normal image $I_N^M := (1 - M_a) \odot I_N$, in which the target anomaly region is removed. Again, these are concatenated to form z_t^{inp} . Now, MGNI injects stochasticity *exclusively* where $M_a = 1$, leaving (normal) background intact. Noise intensity is controlled by a noise scale factor a and time-dependent decay $\lambda(t) = a \mathbb{1}_{t > t_{\min}}$, $t \in [0, 1]$, where $\mathbb{1}$ denotes the indicator function and t is the normalized timestep. Essentially, we let early steps ($t \approx 1$) receive extra noise to diversify texture, while late steps ($t \rightarrow 0$) revert to standard DDIM updates to preserve fidelity. Following DDIM [33], we define $\alpha_t := \prod_{s=1}^t (1 - \beta_s)$ as the cumulative noise schedule, where β_s is a predefined variance schedule. This yields an update that z_{t-1} equals

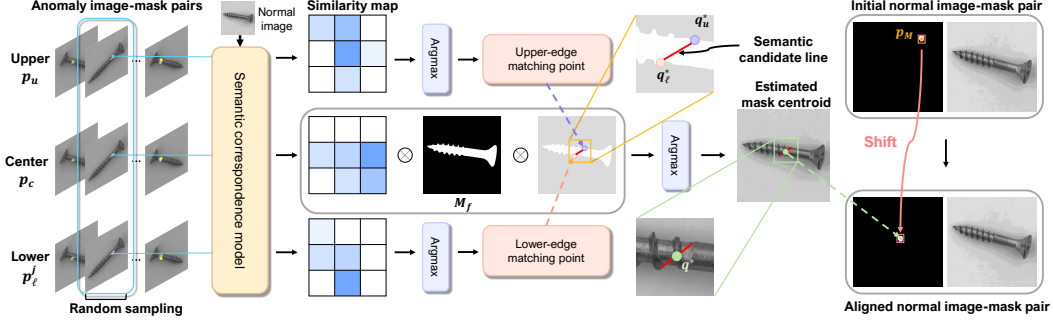


Figure 5: An overview of context-aware mask alignment (CAMA). After sampling an anomaly image-mask pair from the anomaly training set, we automatically select three keypoints, center p_c , upper p_u , and lower p_l , which are on the same vertical line crossing the mask centroid. These points are semantically matched to the normal image to create three similarity maps, S_u , S_c and S_l . The most likely locations of upper and lower points in the normal image (q_u^* and q_l^*) yield a candidate line \mathcal{L} , providing an additional cue for the (mask) center. This constraint along with the object foreground mask M_f and the similarity map S_c is utilized to yield an optimal translated position for the mask.

$$\underbrace{\sqrt{\alpha_{t-1}} \left(\frac{z_t - \sqrt{1 - \alpha_t} \epsilon_\theta(z_t^{\text{inp}}, t, c_p)}{\sqrt{\alpha_t}} \right)}_{\text{DDIM deterministic part}} + \underbrace{\sqrt{1 - \alpha_{t-1}} \epsilon_\theta(z_t^{\text{inp}}, t, c_p)}_{\text{standard DDIM noise}} + \underbrace{\sqrt{1 - \alpha_{t-1}} \sqrt{\lambda(t)} M \eta_t}_{\text{localized noise}},$$

where $\eta_t \sim \mathcal{N}(0, I)$. Confining this extra noise to early timesteps and masked pixels lets MGNI produce diverse but controlled anomaly textures while preserving background integrity (see Fig. 4).

3.4 Context-aware mask alignment (CAMA)

In object-centric categories, such as *screw* or *cable*, anomalies usually appear only in specific, semantically meaningful sub-regions of the object (see Fig. 5). Thus, ensuring that the input anomaly mask is placed in a semantically plausible region is crucial. To achieve this, we propose Context-Aware Mask Alignment (CAMA), which aligns input anomaly masks to appropriate spatial locations on normal images by leveraging semantic correspondences.

We assume access to at least some anomaly training images and their masks at inference. The core intuition is that if reliable keypoint correspondences between an anomaly exemplar and the normal test image can be established, we can transform (mainly via rotation and translation) the exemplar’s mask position into the normal-image coordinate frame. The input mask can then be “snapped” into this aligned position. Dense correspondence networks (e.g., [39]) could do this exhaustively, but running them on every keypoint (patch) of the anomaly image is expensive. Conversely, using only a single keypoint—such as the mask centroid—often fails due to visual discrepancies between anomalous and normal regions yielding substantially different pretrained features such as [24]. CAMA strikes a middle ground: it picks three keypoints per anomaly image (the mask centroid plus two boundary points) providing enough geometric constraint for robust mask transfer while keeping runtime low. We start by sampling a pair of anomaly image I_A and corresponding anomaly mask M_{GT} from the anomaly training set. We then extract three keypoints—center p_c , upper p_u , and lower p_l —sampled from the edge of the (white) anomaly mask region and sharing the same x -coordinate such that they lie on the same vertical line crossing the mask centroid. Using a pretrained semantic correspondence model [39], each keypoint is matched to the normal image, leading to three keypoint similarity maps S_u , S_c and S_l . The most likely upper and lower correspondence points in the normal image are then given as $q_u^* = \arg \max_{(x,y)} S_u(x, y)$ and $q_l^* = \arg \max_{(x,y)} S_l(x, y)$ respectively. Since we know the transformed center point q_c^* must lie on the semantic candidate line \mathcal{L} joining q_u^* and q_l^* , we estimate q_c^* by finding the point which is on the line \mathcal{L} , inside the object foreground mask M_f (extracted using a pretrained U²-Net [25]) and maximizes the score in S_c . In terms of equation,

$$q_c^* = \arg \max_{(x,y) \in \mathcal{L}, M_f(x,y)=1} S_c(x, y), \quad (4)$$

Category	AnomalyDiffusion		AnoGen		DualAnoDiff		MAGIC (Ours)	
	KID ↓	IC-L ↑	KID ↓	IC-L ↑	KID ↓	IC-L ↑	KID ↓	IC-L ↑
bottle	145.46	0.18	135.37	0.17	196.93	0.41	56.75	0.18
cable	97.23	0.41	95.87	0.41	43.48	0.39	40.90	0.39
capsule	106.08	0.19	107.72	0.20	<u>83.18</u>	0.34	27.96	<u>0.22</u>
carpet	108.12	0.23	99.72	0.22	<u>46.39</u>	0.28	36.98	<u>0.26</u>
grid	53.49	0.46	75.64	<u>0.44</u>	48.16	0.39	5.30	0.37
hazelnut	57.62	0.30	64.79	0.31	<u>23.39</u>	0.35	16.78	<u>0.34</u>
leather	<u>215.75</u>	0.38	236.15	0.38	248.13	0.37	159.56	0.33
metal_nut	112.02	0.29	95.13	0.25	46.04	0.30	<u>52.50</u>	0.28
pill	<u>80.03</u>	0.24	94.87	0.23	89.98	0.39	35.98	<u>0.26</u>
screw	<u>10.43</u>	0.30	12.31	0.30	14.22	0.36	3.23	<u>0.32</u>
tile	187.96	<u>0.51</u>	131.52	0.53	<u>95.84</u>	0.45	62.73	0.47
toothbrush	40.10	0.20	<u>38.49</u>	0.15	100.79	0.38	10.92	<u>0.26</u>
transistor	128.18	<u>0.31</u>	183.28	0.40	<u>80.81</u>	0.24	66.08	0.28
wood	63.45	0.35	<u>48.17</u>	0.35	73.70	0.38	38.69	<u>0.37</u>
zipper	<u>154.26</u>	<u>0.24</u>	161.77	<u>0.24</u>	261.33	0.37	74.17	<u>0.24</u>
Average	104.01	0.30	105.39	<u>0.31</u>	<u>96.82</u>	0.36	46.06	0.30

Table 1: Comparison of KID and IC-LPIPS scores. **Bold** and underlined values indicate the best and second-best results in each category. Our method achieves the lowest KID scores, indicating the closest match to the real distribution. While our IC-LPIPS score is lower than that of DualAnoDiff, the higher IC-LPIPS score of DualAnoDiff is partly triggered by corrupted normal background.

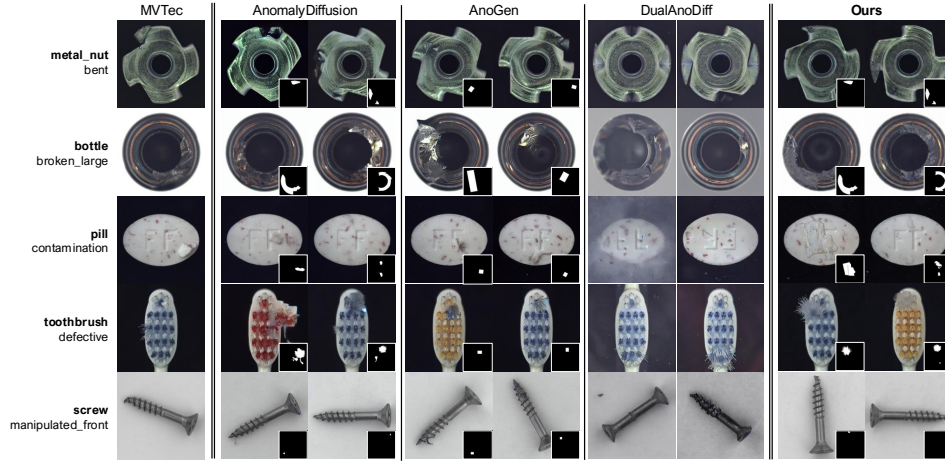


Figure 6: Qualitative comparison of generated anomalies from our model and existing anomaly generation methods. All images are generated under the same setting without any manual filtering.

Then, the initial anomaly mask M is redrawn by moving the centroid of the (white) anomaly mask to q_c^* , resulting in the aligned mask M_a . To ensure the anomaly remains within object regions, we perform logical AND operation between M_a and M_f to yield final M_a .

4 Experimental results

4.1 Experiment settings

Dataset. We evaluated on MVTec-AD [2], which contains 15 industrial categories (10 objects, 5 textures) and 3–8 anomaly types per category (except *toothbrush*, which has one). We adopted the protocol from AnomalyDiffusion [10] to split the training and test sets for anomaly images. More specifically, one-third of the anomaly images per class with round downs are allocated for training and the rest are used for testing. We deliberately avoided the DualAnoDiff split [11], since it can potentially incur an overlap of images in the training set and the test set (see the Appendix for details).

Implementation details. Our framework is based on the Stable Diffusion 2 inpainting model, using a DDIM scheduler with 50 denoising steps during inference. For GPP, we set a fixed noise level $\sigma = 1.0$, uniformly sample the noise scale factor a from $[0, 0.6]$, and use a threshold $t_{\min} = 0.6$. Training is conducted for 5000 steps using AdamW ($lr 5 \times 10^{-6}$), with a batch size of 4 on a single NVIDIA RTX A6000 GPU, requiring about 1.5 hours per anomaly class. Inference takes roughly 1 second per image without CAMA and about 5 seconds with CAMA. Generating results in

Category	Crop-Paste	AnomalyDiffusion	AnoGen	DualAnoDiff	MAGIC (Ours)
bottle	60.47	<u>81.40</u>	62.79	72.09	83.72
cable	37.50	65.62	<u>64.06</u>	56.25	65.62
capsule	<u>49.33</u>	37.33	30.67	48.00	62.67
carpet	<u>64.52</u>	<u>64.52</u>	48.39	70.97	<u>64.52</u>
grid	40.00	40.00	42.50	60.00	<u>55.00</u>
hazelnut	72.92	<u>87.50</u>	68.75	85.42	95.83
leather	52.38	<u>68.25</u>	58.73	84.13	84.13
metal_nut	75.00	<u>82.81</u>	58.33	76.56	87.50
pill	36.46	<u>56.25</u>	37.50	33.33	69.79
screw	39.51	<u>24.69</u>	48.15	<u>58.02</u>	83.95
tile	<u>87.72</u>	<u>87.72</u>	98.25	98.25	98.25
transistor	50.00	75.00	46.43	<u>71.43</u>	<u>71.43</u>
wood	54.76	<u>64.29</u>	73.81	<u>71.43</u>	<u>71.43</u>
zipper	65.85	<u>73.17</u>	58.54	<u>73.17</u>	75.61
Average	56.17	64.90	56.92	<u>68.50</u>	76.39

Table 2: Quantitative comparison of anomaly classification accuracy (%) across different generation methods using ResNet-34 [8]. All results are reproduced under identical evaluation protocol of [10].

Table 1, 2, and 3 takes approximately 1, 0.7, and 1.5 hours per category respectively. For semantic correspondence extraction in CAMA, we use the pretrained GeoAware-SC model [39]. Further implementation details are provided in the Appendix.

Evaluation metrics. To assess the quality and diversity of the generated images, we synthesized 500 anomaly image-mask pairs per class. We measured the Kernel Inception Distance (KID) [3] to evaluate image quality and the Intra-Cluster LPIPS (IC-LPIPS) [23] score to assess diversity among generated samples. Since our training setting involves limited data, we adopted KID instead of Fréchet Inception Distance (FID) [9], as KID provides an unbiased and more reliable estimate in low-data regimes [12]. To validate the effectiveness of the generated data in downstream tasks, we trained a ResNet-34 [8] for anomaly classification, and measured AUROC (Area Under the ROC Curve), AP (Average Precision), and F1-max score for detection and localization performances.

Compared methods. We compare our method with existing anomaly generation approaches, including AnomalyDiffusion, AnoGen, and DualAnoDiff. All baselines are reproduced using their officially released implementations to ensure fair comparison. DefectFill is not included in the main experiments due to its reliance on test-set masks and its limited handling of objects with varying geometric transformations (e.g., rotation or translation) but is partly compared in the appendix. For all methods, including ours, generated anomaly images are evaluated without any filtering or post-processing to reflect their raw generation performance. For classification, we train a classifier using the synthetic samples from each method and include a simple Crop-Paste baseline. For detection and localization, we additionally evaluate PRN, which is tailored for detection tasks. Since PRN leverages external textures (e.g., DTD [4]), it is not directly applicable to classification tasks that require class-specific anomaly patterns. Further implementation details are provided in the Appendix.

4.2 Comparison of anomaly generation results

Figure 6 shows examples of anomaly image-mask pairs generated by each method. Table 1 presents quantitative evaluations of generation fidelity and diversity. We adopt KID to assess how closely the generated images resemble the distribution of real anomalies, where lower values indicate better fidelity. We also use IC-LPIPS, following the setup in DualAnoDiff, to evaluate the diversity of generated images. In our method, anomaly masks are obtained from AnomalyDiffusion and randomly flipped horizontally and vertically before generation. As shown in Table 1, our method reports the lowest KID scores among the compared approaches, which may suggest closer alignment with the real anomaly distribution. Meanwhile, the lower IC-LPIPS score compared to DualAnoDiff could be attributed to background corruptions frequently exhibited by DualAnoDiff as illustrated in Fig. 6.

4.3 Comparison of performances on anomaly downstream tasks

Anomaly classification. To assess the utility of the images generated for downstream tasks, we evaluate anomaly classification accuracy using images synthesized by our method. Following the experimental setup of AnomalyDiffusion, we train a ResNet-34 [8] on the generated samples. As shown in Table 2, our method shows improved classification accuracy compared to other baselines. This result suggests that the combination of semantic alignment and the use of multi-level perturbation

Category	Crop-Paste				PRN				AnomalyDiffusion				AnoGen				DualAnoDiff				MAGIC (Ours)			
	AUC-P	AP-P	F1-P	AP-I	AUC-P	AP-P	F1-P	AP-I	AUC-P	AP-P	F1-P	AP-I	AUC-P	AP-P	F1-P	AP-I	AUC-P	AP-P	F1-P	AP-I	AUC-P	AP-P	F1-P	AP-I
bottle	97.5	86.0	79.4	99.7	99.1	89.4	82.2	99.5	99.3	92.6	84.6	99.8	98.0	83.0	74.5	99.7	98.7	88.4	81.4	100.0	99.7	96.1	89.5	100.0
cable	91.1	38.4	80.8	98.5	97.9	83.3	77.3	99.4	98.4	84.3	76.3	99.9	94.8	68.3	64.7	98.6	91.3	72.9	69.9	99.0	98.2	82.1	75.4	98.4
capsule	97.8	86.6	45.2	99.2	96.5	47.9	52.3	98.8	97.9	41.6	43.7	98.9	96.3	34.0	37.5	99.3	98.8	47.8	52.8	99.0	98.9	62.3	62.4	99.1
carpet	94.4	65.9	61.9	96.7	95.5	63.4	61.7	98.2	96.4	74.8	71.8	97.5	98.8	81.4	74.0	98.1	99.1	87.1	78.5	99.6	98.8	86.1	79.0	98.6
grid	89.8	35.7	36.9	97.4	<u>97.7</u>	54.5	54.8	98.2	97.3	43.6	46.0	<u>99.3</u>	96.1	33.1	41.8	99.2	95.4	<u>54.9</u>	<u>55.0</u>	<u>99.3</u>	99.4	57.1	58.0	99.9
hazelnut	99.1	86.8	78.8	99.8	99.8	92.6	85.5	98.5	99.3	89.4	81.9	100.0	97.2	58.3	56.7	99.7	<u>99.5</u>	88.7	81.0	<u>99.9</u>	99.8	97.0	91.4	100.0
leather	96.9	63.6	66.1	99.3	98.1	64.9	64.2	99.9	99.8	78.4	<u>71.0</u>	100.0	99.4	77.7	70.4	100.0	99.8	82.8	73.6	100.0	<u>99.7</u>	81.4	73.6	100.0
metal_nut	99.6	98.6	94.7	100.0	99.8	98.7	94.7	100.0	99.6	97.8	92.5	100.0	95.2	77.0	72.5	99.9	99.5	96.7	91.8	99.8	99.9	99.3	96.0	100.0
pill	99.3	95.6	87.7	99.7	<u>99.7</u>	<u>95.7</u>	<u>89.2</u>	99.2	99.6	95.0	88.5	99.5	99.2	89.1	80.7	99.1	97.1	83.0	77.9	97.4	99.9	97.7	92.3	99.9
screw	97.4	40.0	44.5	<u>97.5</u>	<u>97.8</u>	37.9	41.0	95.9	95.6	11.8	21.6	96.9	92.7	21.9	27.2	96.1	98.2	<u>50.4</u>	<u>51.2</u>	91.3	97.6	52.8	52.2	98.3
tile	99.4	96.2	89.3	99.9	99.5	96.0	90.6	99.7	99.5	96.0	88.9	100.0	99.2	93.1	85.0	100.0	99.6	95.4	89.2	100.0	99.8	97.8	92.2	100.0
toothbrush	74.2	31.3	41.2	97.7	98.5	56.9	61.1	100.0	97.9	56.6	58.5	99.3	99.2	93.1	85.0	100	93.8	56.2	60.9	96.3	99.4	<u>73.5</u>	<u>73.4</u>	99.5
transistor	88.6	68.3	76.5	97.5	97.1	83.8	81.0	99.2	99.2	89.1	81.2	100.0	95.0	63.2	61.2	98.8	92.5	73.9	71.1	98.1	94.8	62.9	60.3	100.0
wood	97.1	74.0	74.4	100.0	97.9	78.8	74.0	99.3	96.7	74.6	67.4	<u>99.9</u>	<u>98.5</u>	78.2	71.5	99.5	98.3	<u>84.6</u>	<u>77.2</u>	<u>99.9</u>	99.5	91.0	82.4	99.0
zipper	93.9	70.7	74.3	<u>99.5</u>	98.5	80.4	76.2	100.0	<u>99.4</u>	<u>84.7</u>	<u>78.2</u>	100.0	99.1	78.9	71.8	100.0	99.5	89.0	82.0	100.0	99.2	89.0	82.2	100.0
Average	94.4	69.1	70.7	98.9	98.2	75.0	<u>73.2</u>	99.1	<u>98.4</u>	74.0	70.1	<u>99.4</u>	96.2	64.2	61.6	99.2	97.4	<u>76.8</u>	72.9	98.6	99.0	81.7	77.4	99.5

Table 3: Comparison of anomaly detection (AP-I) and anomaly localization (AUC-P, AP-P, F1-P) results obtained with U-Net [27]. All results are reproduced under identical evaluation protocol [10].

GPP	MGNI	CAMA	KID ↓			IC-LPIPS ↑			Classification Acc. ↑		
			Object	Texture	Average	Object	Texture	Average	Object	Texture	Average
×	×	×	40.36	63.20	47.97	0.273	0.346	0.298	70.09	71.10	70.45
✓	×	×	33.87	57.17	41.64	0.274	0.354	0.301	74.07	71.94	73.31
✓	✓	×	40.13	<u>60.65</u>	46.84	0.285	0.359	0.310	<u>74.50</u>	74.66	<u>74.56</u>
✓	✓	✓	<u>38.76</u>	<u>60.65</u>	<u>46.06</u>	<u>0.277</u>	0.359	<u>0.304</u>	77.35	74.66	76.39

Table 4: Ablation study on the effects of GPP, MGNI, and CAMA.

contributes to a better classification outcomes. Specifically, the classifier trained on our images yields an average accuracy that is 7.89% higher than that of previous state-of-the-art (DualAnoDiff).

Anomaly detection and localization. We evaluate the effectiveness of our generated data for anomaly detection and localization, comparing results with Crop-Paste, PRN, AnomalyDiffusion, AnoGen, and DualAnoDiff. Each method generates 500 anomaly image-mask pairs, used to train a U-Net segmentation model [27] following the protocol established by AnomalyDiffusion [10] and DualAnoDiff [11]. We report pixel-level metrics (AUROC-P, AP-P, F1-P) and the image-level metric (AP-I) in Table 3; additional image-level results (AUROC-I, F1-max) are provided in the Appendix. Our approach achieves AUROC-P of 99.0%, AP-P of 81.7%, F1-max of 77.4%, and AP-I of 99.5%, showing consistent improvements across the evaluated metrics compared to the baseline methods.

4.4 Ablation study

We conduct an ablation study to evaluate the individual contributions of GPP, MGNI, and CAMA to the overall performance of our framework. Results are summarized in Table 4. Introducing GPP alone significantly reduces the KID scores, demonstrating enhanced generalization, and subsequently improves classification accuracy by approximately 2.86%. Although adding MGNI slightly increases the KID scores due to enhanced diversity, it facilitates the generation of images beneficial for downstream tasks, improving overall classification performance. Incorporating both GPP and MGNI also leads to better IC-LPIPS scores and provides additional accuracy gains of about 4.41% for object categories and 3.56% for texture categories. Finally, applying CAMA notably enhances object-level fidelity, as evidenced by further reduced object-class KID scores, and contributes to an additional accuracy increase of approximately 2.85% on average for the object classes. These results confirm that our alignment module successfully enforces structural consistency between the synthesized anomalies and the surrounding normal context, thereby enhancing classification performance.

5 Conclusion

We presented MAGIC, a mask-guided diffusion framework that tackles three persistent failures of current few-shot anomaly generators: (i) corrupted backgrounds, (ii) poor mask-defect overlap, and (iii) defects placed in semantically implausible regions. MAGIC starts with a Stable Diffusion inpainting backbone to keep the background intact and respect the input mask, then restores lost diversity through two multi-level perturbations: Gaussian Prompt Perturbation (GPP) for global appearance variation and Mask-Guided Noise Injection (MGNI) for local textural richness. To ensure spatial plausibility, the Context-Aware Mask Alignment (CAMA) module realigns masks using lightweight semantic correspondences. Extensive ablations and benchmark tests on MVTec-

AD confirm that MAGIC achieves improved balance of image fidelity and diversity leading to state-of-the-art results in downstream anomaly detection, localization, and classification.

Limitations. CAMA works best when the input mask roughly matches the typical shape and location of real defects; large deviations reduce correspondence accuracy and can misalign the mask. Also, our pipeline also inherits error modes from its pretrained parts—U²-Net for foregrounds and GeoAware-SC for correspondences—so visually ambiguous (e.g. due to repetitive structures) or unseen domains may yield imperfect anomaly placement.

Broader impacts. This work may contribute to improved visual inspection systems by enabling realistic anomaly synthesis from limited data. However, synthetic defects could be potentially misused to manipulate inspection outcomes, highlighting the need for responsible and controlled deployment.

References

- [1] Musawar Ali, Nicola Fioraio, Samuele Salti, and Luigi Di Stefano. Anomalycontrol: Few-shot anomaly generation by controlnet inpainting. *IEEE Access*, 12:192903–192914, 2024.
- [2] Paul Bergmann, Michael Fauser, David Sattlegger, and Carsten Steger. Mvtec ad—a comprehensive real-world dataset for unsupervised anomaly detection. In *IEEE/CVF Conference on Computer Vision and Pattern Recognition (CVPR)*, pages 9592–9600, 2019.
- [3] Mikolaj Binkowski, Danica J. Sutherland, Michal Arbel, and Arthur Gretton. Demystifying mmd gans. *ArXiv*, abs/1801.01401, 2018.
- [4] Mircea Cimpoi, Subhransu Maji, Iasonas Kokkinos, Sammy Mohamed, and Andrea Vedaldi. Describing textures in the wild. In *IEEE Conference on Computer Vision and Pattern Recognition (CVPR)*, June 2014.
- [5] Yuxuan Duan, Y. Hong, Li Niu, and Liqing Zhang. Few-shot defect image generation via defect-aware feature manipulation. In *AAAI Conference on Artificial Intelligence*, 2023.
- [6] Rinon Gal, Yuval Alaluf, Yuval Atzmon, Or Patashnik, Amit H. Bermano, Gal Chechik, and Daniel Cohen-Or. An image is worth one word: Personalizing text-to-image generation using textual inversion. *ArXiv*, abs/2208.01618, 2022.
- [7] Guan Gui, Bin-Bin Gao, Jun Liu, Chengjie Wang, and Yunsheng Wu. Few-shot anomaly-driven generation for anomaly classification and segmentation. In *European Conference on Computer Vision (ECCV)*, 2024.
- [8] Kaiming He, Xiangyu Zhang, Shaoqing Ren, and Jian Sun. Deep residual learning for image recognition. In *2016 IEEE Conference on Computer Vision and Pattern Recognition (CVPR)*, pages 770–778, 2016. doi: 10.1109/CVPR.2016.90.
- [9] Martin Heusel, Hubert Ramsauer, Thomas Unterthiner, Bernhard Nessler, Günter Klambauer, and Sepp Hochreiter. Gans trained by a two time-scale update rule converge to a nash equilibrium. *ArXiv*, abs/1706.08500, 2017.
- [10] Teng Hu, Jiangning Zhang, Ran Yi, Yuzhen Du, Xu Chen, Liang Liu, Yabiao Wang, and Chengjie Wang. Anomalydiffusion: Few-shot anomaly image generation with diffusion model. In *AAAI Conference on Artificial Intelligence*, 2023.
- [11] Ying Jin, Jinlong Peng, Qingdong He, Teng Hu, Jiafu Wu, Hao Chen, Haoxuan Wang, Wenbing Zhu, Mingmin Chi, Jun Liu, and Yabiao Wang. Dual-interrelated diffusion model for few-shot anomaly image generation. *arXiv preprint arXiv:2408.13509*, 2024.
- [12] Tero Karras, Miika Aittala, Janne Hellsten, Samuli Laine, Jaakko Lehtinen, and Timo Aila. Training generative adversarial networks with limited data. *Advances in Neural Information Processing Systems*, 33:12104–12114, 2020.
- [13] Tero Karras, Samuli Laine, Miika Aittala, Janne Hellsten, Jaakko Lehtinen, and Timo Aila. Analyzing and improving the image quality of stylegan. *IEEE/CVF Conference on Computer Vision and Pattern Recognition (CVPR)*, pages 8107–8116, 2020.
- [14] Naveen Kodali, Jacob D. Abernethy, James Hays, and Zsolt Kira. How to train your dragan. *ArXiv*, abs/1705.07215, 2017.
- [15] Nupur Kumari, Bin Zhang, Richard Zhang, Eli Shechtman, and Jun-Yan Zhu. Multi-concept customization of text-to-image diffusion. *IEEE/CVF Conference on Computer Vision and Pattern Recognition (CVPR)*, pages 1931–1941, 2022.

- [16] Chun-Liang Li, Kihyuk Sohn, Jinsung Yoon, and Tomas Pfister. Cutpaste: Self-supervised learning for anomaly detection and localization. *IEEE/CVF Conference on Computer Vision and Pattern Recognition (CVPR)*, pages 9659–9669, 2021.
- [17] Dongyun Lin, Yanpeng Cao, Wenbin Zhu, and Yiqun Li. Few-shot defect segmentation leveraging abundant normal training samples through normal background regularization and crop-and-paste operation. *ArXiv*, abs/2007.09438, 2020.
- [18] Jiang Lin and Yaping Yan. A comprehensive augmentation framework for anomaly detection. In *AAAI Conference on Artificial Intelligence*, volume 38, pages 8742–8749, 2024.
- [19] Hongyu Liu, Ziyu Wan, Wei Huang, Yibing Song, Xintong Han, and Jing Liao. Pd-gan: Probabilistic diverse gan for image inpainting. *IEEE/CVF Conference on Computer Vision and Pattern Recognition (CVPR)*, pages 9367–9376, 2021.
- [20] Lars M. Mescheder, Andreas Geiger, and Sebastian Nowozin. Which training methods for gans do actually converge? In *International Conference on Machine Learning*, 2018.
- [21] Alex Nichol, Prafulla Dhariwal, Aditya Ramesh, Pranav Shyam, Pamela Mishkin, Bob McGrew, Ilya Sutskever, and Mark Chen. Glide: Towards photorealistic image generation and editing with text-guided diffusion models. In *International Conference on Machine Learning*, 2021.
- [22] Shuanlong Niu, Bin Li, Xinggang Wang, and Hui Lin. Defect image sample generation with gan for improving defect recognition. *IEEE Transactions on Automation Science and Engineering*, PP:1–12, 02 2020.
- [23] Utkarsh Ojha, Yijun Li, Jingwan Lu, Alexei A. Efros, Yong Jae Lee, Eli Shechtman, and Richard Zhang. Few-shot image generation via cross-domain correspondence. *IEEE/CVF Conference on Computer Vision and Pattern Recognition (CVPR)*, pages 10738–10747, 2021.
- [24] Maxime Oquab, Timothée Darcet, Theo Moutakanni, Huy V. Vo, Marc Szafraniec, Vasil Khalidov, Pierre Fernandez, Daniel Haziza, Francisco Massa, Alaaeldin El-Nouby, Russell Howes, Po-Yao Huang, Hu Xu, Vasu Sharma, Shang-Wen Li, Wojciech Galuba, Mike Rabbat, Mido Assran, Nicolas Ballas, Gabriel Synnaeve, Ishan Misra, Herve Jegou, Julien Mairal, Patrick Labatut, Armand Joulin, and Piotr Bojanowski. Dinov2: Learning robust visual features without supervision, 2023.
- [25] Xuebin Qin, Zichen Zhang, Chenyang Huang, Masood Dehghan, Osmar R Zaiane, and Martin Jägersand. U2-net: Going deeper with nested u-structure for salient object detection. *Pattern Recognition*, 106:107404, 2020.
- [26] Robin Rombach, A. Blattmann, Dominik Lorenz, Patrick Esser, and Björn Ommer. High-resolution image synthesis with latent diffusion models. *IEEE/CVF Conference on Computer Vision and Pattern Recognition (CVPR)*, pages 10674–10685, 2021.
- [27] Olaf Ronneberger, Philipp Fischer, and Thomas Brox. U-net: Convolutional networks for biomedical image segmentation. In Nassir Navab, Joachim Hornegger, William M. Wells, and Alejandro F. Frangi, editors, *Medical Image Computing and Computer-Assisted Intervention – MICCAI 2015*, pages 234–241, Cham, 2015. Springer International Publishing. ISBN 978-3-319-24574-4.
- [28] Karsten Roth, Latha Pemula, Joaquin Zepeda, Bernhard Scholkopf, Thomas Brox, and Peter Gehler. Towards total recall in industrial anomaly detection. *IEEE/CVF Conference on Computer Vision and Pattern Recognition (CVPR)*, pages 14298–14308, 2022.
- [29] Nataniel Ruiz, Yuanzhen Li, Varun Jampani, Yael Pritch, Michael Rubinstein, and Kfir Aberman. Dream-booth: Fine tuning text-to-image diffusion models for subject-driven generation. In *Proceedings of the IEEE/CVF Conference on Computer Vision and Pattern Recognition (CVPR)*, pages 10684–10694, 2023.
- [30] Seyedmorteza Sadat, Jakob Buhmann, Derek Bradley, Otmar Hilliges, and Romann M. Weber. Cads: Unleashing the diversity of diffusion models through condition-annealed sampling. *ArXiv*, abs/2310.17347, 2023.
- [31] Chitwan Saharia, William Chan, Saurabh Saxena, Lala Li, Jay Whang, Emily L. Denton, Seyed Kam-yar Seyed Ghasemipour, Burcu Karagol Ayan, Seyedeh Sara Mahdavi, Raphael Gontijo Lopes, Tim Salimans, Jonathan Ho, David J. Fleet, and Mohammad Norouzi. Photorealistic text-to-image diffusion models with deep language understanding. *ArXiv*, abs/2205.11487, 2022.
- [32] Jaewoo Song, Daemin Park, Kanghyun Baek, Sangyub Lee, Jooyoung Choi, Eunji Kim, and Sungroh Yoon. Defectfill: Realistic defect generation with inpainting diffusion model for visual inspection. *ArXiv*, abs/2503.13985, 2025.

- [33] Jiaming Song, Chenlin Meng, and Stefano Ermon. Denoising diffusion implicit models. *arXiv:2010.02502*, October 2020.
- [34] Cairong Wang, Yiming Zhu, and Chun Yuan. Diverse image inpainting with normalizing flow. In *European Conference on Computer Vision*, 2022.
- [35] Jing Wei, Zhengtao Zhang, Fei Shen, and Chengkan Lv. Mask-guided generation method for industrial defect images with non-uniform structures. *Machines*, 10(12):1239, 2022. doi: 10.3390/machines10121239.
- [36] Vitjan Zavrtanik, Matej Kristan, and Danijel Skocaj. Draem – a discriminatively trained reconstruction embedding for surface anomaly detection. *IEEE/CVF International Conference on Computer Vision (ICCV)*, pages 8310–8319, 2021.
- [37] Gongjie Zhang, Kaiwen Cui, Tzu-Yi Hung, and Shijian Lu. Defect-gan: High-fidelity defect synthesis for automated defect inspection. *IEEE Winter Conference on Applications of Computer Vision (WACV)*, pages 2523–2533, 2021.
- [38] Hui Min Zhang, Zuxuan Wu, Z. Wang, Zhineng Chen, and Yu-Gang Jiang. Prototypical residual networks for anomaly detection and localization. *IEEE/CVF Conference on Computer Vision and Pattern Recognition (CVPR)*, pages 16281–16291, 2022.
- [39] Junyi Zhang, Charles Herrmann, Junhwa Hur, Eric Chen, Varun Jampani, Deqing Sun, and Ming-Hsuan Yang. Telling left from right: Identifying geometry-aware semantic correspondence. In *IEEE/CVF Conference on Computer Vision and Pattern Recognition (CVPR)*, 2024.
- [40] Lingrui Zhang, Shuheng Zhang, Guoyang Xie, Jiaqi Liu, Hua Yan, Jinbao Wang, Feng Zheng, and Yaochu Jin. What makes a good data augmentation for few-shot unsupervised image anomaly detection? In *IEEE/CVF conference on computer vision and pattern recognition*, pages 4345–4354, 2023.
- [41] Lvmin Zhang, Anyi Rao, and Maneesh Agrawala. Adding conditional control to text-to-image diffusion models. *IEEE/CVF International Conference on Computer Vision (ICCV)*, pages 3813–3824, 2023.
- [42] Brian Nlong Zhao, Yuhang Xiao, Jiashu Xu, Xinyang Jiang, Yifan Yang, Dongsheng Li, Laurent Itti, Vibhav Vineet, and Yunhao Ge. Dreamdistribution: Learning prompt distribution for diverse in-distribution generation. In *Proceedings of the International Conference on Learning Representations (ICLR)*, 2025.
- [43] Fanbo Zhu, Zekun Liu, Yue Zhang, and Ziwei Liu. Few-shot image generation with diffusion models. *arXiv preprint arXiv:2210.04584*, 2022.